Multifunctional ZnO-Co_3O_4 @ polymer hybrid nanocoatings with controlled adsorption, photocatalytic and anti-microbial function for polluted water systems

Qurat Ul Ain Nadeem[1,2], Zoobia Nadeem [1], Rohama Gill[*1], Dmitry G. Shchukin[*2]

[1]Fatima Jinnah Women University, The Mall, Rawalpindi, Pakistan

[2]Stephenson Institute for Renewable Energy, University of Liverpool, UK

**Corresponding authors:*

Rohama Gill: rohama_gill@hotmail.com

Dmitry G. Shchkuin: d.shchukin@liverpool.ac.uk

Abstract

Triple action pollutant responsive multi-layer hybrid nanocoatings of architecture PEI(PAA/ZnO-$Co_3O_4)_n$ were constructed through ZnO-Co_3O_4 binary oxide co-precipitation followed by its inclusion in multi-layer polymeric thin films using Layer-by-Layer (LbL) deposition. Characterization of the designed architecture was carried out *via* FTIR, XRD, UV-Vis and Raman spectroscopic studies to evaluate the chemical nature, bonding and crystallographic behavior of ZnO-Co_3O_4. Peaks of ZnO-Co_3O_4 were recorded at 586.38, 486.08 and 443.64cm^{-1} while pronounced shifting of ZnO characteristic E_2 (high) peak ~450cm^{-1} and appearance of modes around 495, 530, 630 and 719cm^{-1} indexed via Raman studies validated Co_3O_4 impregnation into ZnO structure. XRD patterns of ZnO-Co_3O_4 compared to their previously reported pristine structures also justified the formation of binary oxide as unit composite. SEM micrographs confirmed homogenous multilayered depositions while EDX analysis confirmed their uniform elemental distribution in the unit structure. Sequential multilayer buildup of the architecture was monitored using Ellipsometry and UV-Vis with a maximum film thickness ~89nm and UV-Vis absorbance at 376nm were recorded as a function of 48 layer pair depositions. FAAS, ICP-OES, and UV-Vis spectroscopy analyses make these multifunctional hybrid nanocoatings promising for industrial wastewater as well as drinking water purification setups. Furthermore, protuberant recycling and regenerative capacity makes these hybrid nanocoatings an eco-friendly system for hydro-remediation.

Key words: Hybrid nanocoatings; Wastewater treatment; LbL; Ellipsometry; Raman spectroscopy; ICP-OES.

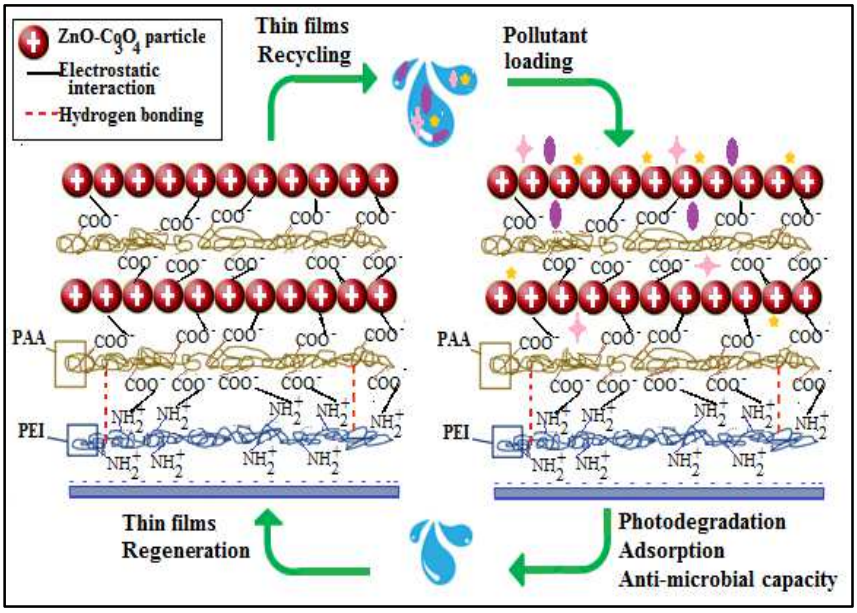

Graphical Abstract

Introduction

A combination of organic/inorganic nano-sized moieties broadly categorized as 'hybrid nanomaterials' has gained considerable attention in nanotechnology research due to the tailored properties and wider applications we can exploit from them. It is only in previous years that this class of materials has started gaining room to provide cost-effective and green solutions for rapidly deteriorating environmental conditions, particularly that of hydrological sector. Hybrid nanomaterials in various combinations including polymer/metal, polymer/ceramic, polymer/carbon nanotubes, and polymer/metal oxide, have been explored to devise adsorbents, photocatalysts, anti-microbial agents for polluted water systems. Different methodologies have been applied to incorporate inorganic fillers into a polymer matrices. These methods include chemical methods such as *in situ* polymerization involving spontaneous nanoparticle formation as well as physical methods such as solvent casting or spin coating (Li et al. 2010; Katheresan et al. 2018; Gołąbiewska et al. 2018). Immobilization of inorganic nanoparticles into organic polymeric layers on solid support is an attractive technique for improving cost-effectiveness, reducing raw material consumption, ensuring convenient recollection and recycling, and reducing physical impairment (Pedanekar et al. 2020). In this regard, Layer-by-Layer (LbL) deposition technique is a green approach which has several advantages over other techniques such as control on the amount of organic/inorganic nanomaterial, enhanced reusability of the raw materials as well as the product, ambient temperature requirements, and most importantly ease in design and operation (Gill et al. 2010; Batool et al. 2018 ; Batool et al. 2020). This technique involves the buildup of multilayers on a substrate by alternate dipping in oppositely charged polyelectrolyte solutions via physical adsorption (Decher 1997; Mahlambi et al. 2015). Despite the benefits of LbL fabrication technique, only one study has been reported so far by Gokul et al. (2017), for the fabrication of binary metal oxide films for treatment of dye laden wastewater. This could be attributed to the fact that most of the generated literature on utilization of metal oxides for wastewater remediation is oriented towards the synthesis and application of metal oxide powder/nanoparticles in its sole form. Thus, with the discovery of the effectiveness of titanium dioxide (TiO_2) to remediate polluted water, intensive research has been conducted to evaluate its photocatalytic, adsorbent and anti-microbial properties along with other metal oxides including zinc oxide (ZnO) (Lee et al. 2016; Kumar & Rao 2015). With further advancement in research, coupling of metal oxides as binary or tertiary oxides has become a prominent research area as it leads to obtain the desired

beneficial properties from the oxides of the combined metals in better proportion. It has been reported that the water remediation activity (photocatalysis, adsorption, anti-microbial action) of TiO_2 and ZnO is enhanced upon coupling with some metal oxides such as silicon oxide (SiO_2) (Guo et al. 2014), cerium oxide (CeO_2) (Ameen et al. 2014), tungsten oxide (WO_3) (Anandan et al. 2014; Patil et al. 2019), and iron oxide (Fe_2O_3) (Abbas et al. 2016). Thus, considering the synthesis of polymer/metal oxide based novel hybrid nanocomposites for wastewater remediation, there`s much room not only in exploring mixed metal oxide/ polymer based novel combinations but utilizing state-of-the-art fabrication techniques like LbL deposition technique to devise novel hybrid nanocomposites with tailored properties depending on the requirement of the end-user.

In the present work, we report the synthesis of binary metal oxide composites and fabrication of polyelectrolyte incorporated ZnO-Co_3O_4 hybrid thinfilms for their 3 in 1 pollutant remediation application against the three major classes of water pollutants i.e. synthetic dyes, heavy metals, and bacterial pathogens from polluted water systems. To the best of our knowledge, the currently designed multi-layer architecture PEI(PAA/ZnO-Co_3O_4)$_n$ is novel in its kind as no work has been reported so far on such `triple action hybrid thin films` as nanofilters for water remediation systems. Furthermore, the efficient recyclability and long-term usage studies of the prepared nanofilters make them promising for their futuristic application as green alternatives for industrial wastewater treatment.

Experimental

Materials

In the current study, following analytically pure reagents were employed as received: Zinc acetate dihydrate ($Zn(CH_3COO)_2$. $2H_2O$), methanol (CH_3OH), polyacrylic acid solution (PAA) (M_w-~250,000 g/mol; 35% in water), hydrochloric acid (HCl) (37%), polyethylene imine (PEI) (M_w-~25,000 g/mol), sodium chloride (NaCl), and sulfuric acid (H_2SO_4) (95-97%) were purchased from Sigma-Aldrich®; cobalt acetate tetrahydrate ($Co(CH_3COO)_2$. $4H_2O$) and copper sulphate penta hydrate ($CuSO_4$. $5H_2O$) were procured from Merck; sodium hydroxide (NaOH) was obtained from Riedel de Haen; and Methylene Blue, was purchased from BDH chemicals.

Method

Phase I: Synthesis of ZnO-Co_3O_4 composites

Composites of ZnO with varied concentrations (conc.) of Co_3O_4 were synthesized *via* co-precipitation method. Appropriate amounts of precursor salts were dissolved in mixed solvent (distilled water and methanol) followed by dropwise addition of 2.5M methanolic NaOH solution under constant stirring conditions (until pH>10). Precipitates obtained from this process were filtrated, washed, oven dried (at 110^{o}C for 1hr) and then calcined in muffle furnace (at 700^{o}C for 3 hr). Similar procedure was followed to synthesize binary oxides of ZnO-Co_3O_4 with 1, 3, 5,7, and 9 wt.% Co_3O_4.

Phase II: Multilayer build-up of PEI(PAA/ZnO-Co_3O_4)$_n$ thin films

Thin films with architecture PEI(PAA/ZnO-Co_3O_4)$_n$ were fabricated using the procedure adopted by Gill et al., 2010, with few modifications. Glass slide (20mm*20mm) and silicon wafer (10mm*40mm) substrates were etched by immersion in a mixture of CH_3OH and HCl (1:1), followed by dipping in H_2SO_4 overnight. Suspensions of ZnO-Co_3O_4 composites in DW were made *via* sonication for 10 min. PEI (2 mg/mL) and PAA (2 mg/mL) were prepared in distilled water and 0.1M NaCl solution, respectively.

Multilayer thin films were fabricated on the etched glass and silicon substrates as well as on cellulose acetate membrane filters (3.0 µm) by immersion in polycation (PEI) solution for 15 minutes, followed by alternate immersion in polyanion (PAA) solution (10 min) and ZnO-Co_3O_4 suspension for appropriate time period. Each deposition step was followed by drying with a stream of N_2 gas and three washes in distilled water (2 min each) to remove unreacted species. The described procedure was repeated to achieve the desired number of layer pairs. Influence of various parameters on deposition of thin films was investigated and discussed in detail under UV-Vis studies section.

Characterization techniques

In current study, functional groups of binary metal oxide powders were determined using a Fourier Transform Infrared Spectrometer (Shimadzu 8400) by KBr pellet method in the wavenumber range of 4000-400 cm^{-1}. Thermogravimetric analysis was conducted using PERKIN ELMER TGA. Crystalline structure of the binary metal oxide composite was studied using PANalytical X-ray diffractometer (XPERT PRO). Raman shifts were recorded using Horiba, XploRA plus. Instrument was calibrated with objective lens × 50 LWD , grating ~ 1800gr/mm, and with 532 nm laser. Morphological behavior and elemental compositions of the prepared binary metal oxides and their deposited thin films were studied using instrument JEOL 6610 SEM coupled with Oxford INCA X-act EDX detector with INCA software. Growth of polyelectrolyte incorporated binary metal oxide thin films on glass substrate was monitored using UV-Visible spectrophotometer (UV-1602 Biotechnology Medical Services) and (Thermoscientific evolution 201) while, Ellipsometer (SE 400adv, Sentech, GmbH) was used for film thickness measurement of thinfilms deposited on silicon wafer at wavelength 632 nm, refractive index of 1.456, and constant incident angle of 70^{o}. UV-1602 Biotechnology Medical Services was used to evaluate the photocatalytic efficiency of designed thinfilms. For MB dye photodegradation studies, the system was then exposed to UV radiation (365 nm) using an 8 W UV lamp. Flame atomic absorption spectrometry (FAAS) (AA220, Varian Inc. Australia) was used to analyze Cu (II) concentration in the solution before and after the equilibrium. Study of Cu (II) concentration in the solution before and after the equilibrium was also performed via inductively coupled plasma - optical emission spectrometry (ICPE-OES) on the instrument, MY16270003. For antimicrobial testing, broth microdilution technique was used to test bactericidal efficiency of the prepared nanocoatings deposited on glass substrate. UV-Vis spectrophotometer (UV-1602, Biotechnology Medical Services) was used for optical density measurements of the control (broth + *E. coli*) and sample (broth + *E. coli* + prepared thin films) that were recorded at OD_{600nm} as a function of time.

Results and Discussion

Fourier-transform infrared spectroscopic (FTIR) analysis of ZnO-Co_3O_4 binary metal oxide

Fourier-transform infrared spectroscopy (FTIR) spectrum of the prepared mixed metal oxides was recorded in solid phase using KBr pellet technique in the range of 4000-400 cm^{-1}. Fig. 1 corresponds to the FTIR spectra of pristine ZnO, Co_3O_4, and ZnO-Co_3O_4 mixed metal oxides with varied wt.% of Co_3O_4 where a clear picture of the particular chemical bonds and fingerprint regions confirms the composition and quality of the product obtained from the opted synthetic procedure Absorption bands in the range of 453.29-875.71 cm^{-1} are assigned to interionic vibrations of binary metal oxide composites (Bodke et al. 2018; Hassan et al. 2017; Azurdia et al. 2006). Whereas bands in the range 1024.24-1097.53 cm^{-1}, 2852.81-2962.76 cm^{-1}, and at 3446.2 cm^{-1} are attributed to C-O, C-H stretching and O-H vibrations, respectively (Hsieh 2007; Azurdia et al. 2006). The appearance of a shoulder near 586.38 cm^{-1} was observed with the increase in Co_3O_4 loading from 1wt.% to 7 wt.% as shown in fig. 1. Furthermore, double absorption bands were also observed in the spectra which indicate the formation of pure binary metal oxide composites, also reported by Abraham et al. (2018). FTIR overlay of the pristine ZnO in the range 400-550cm^{-1} (Yusan et al. 2015) and that of pristine Co_3O_4 at 584.45 cm^{-1} and 673.18 cm^{-1} (Tang et al. 2008), also confirm the formation of binary oxides when compared with the ZnO-Co_3O_4 with varied wt.% of Co_3O_4 in prepared samples.

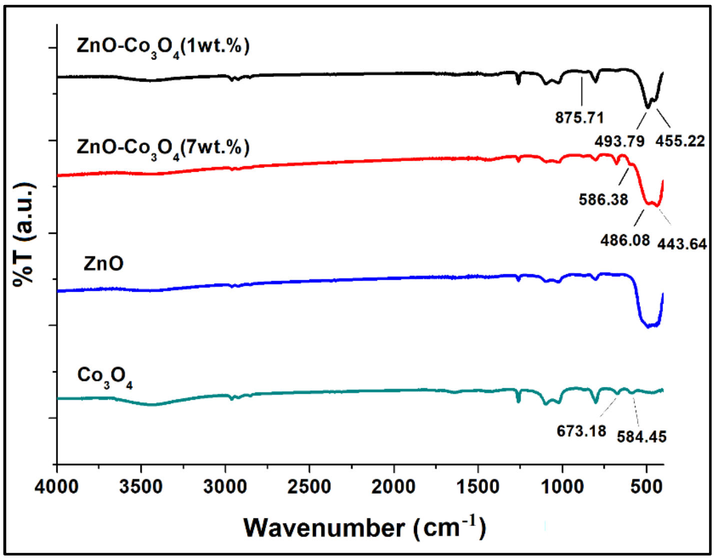

Fig .1 Fourier-transform infrared spectroscopic (FTIR) analysis of pristine ZnO, Co_3O_4 and their varied wt.% in ZnO-Co_3O_4 powder

X-ray diffraction (XRD) analysis of ZnO-Co_3O_4 binary metal oxide

X-ray diffraction (XRD) analysis was carried out to study crystallographic nature of ZnO-Co_3O_4. The crystallite size measurements were carried out by using Debye-Scherer`s equation (eq.1)

$$D = \frac{K\lambda}{\beta\cos\theta} \quad \text{...} \quad \text{(eq.1)}$$

Where, D corresponds to crystallite size (nm), λ is the X-ray wavelength (nm), K is Scherrer's constant usually taken as 0.9, β is angular width expressed in radians and θ is the Bragg's angle (deg).

Diffraction pattern of ZnO-Co_3O_4 represented in Fig. 2 was recorded between of 10 and 80 2θ degree (XRD pattern of 7 wt.% Co_3O_4 in ZnO optimized w.r.t. UV-Vis studies conducted for layer pair growth has been selected for discussion). Significant 2θ peaks at 31.27°, 31.59°, 34.22°, 36.13°, 36.85°, 47.43°, 56.35°, 59.35°, 62.77°, 65.23°, 66.29°, 67.81°, 68.97°, and 76.83° were recorded as a result of diffraction studies of ZnO-Co_3O_4. Peak positions at 31.59°, 34.22°, 36.13°, 47.43°, 56.35°, 62.77°, 66.29°, 67.81°, and 68.97° correspond to (100), (002), (101), (102), (110), (103), (200), (112), (201) planes of ZnO, respectively. However, 2θ = 31.27°, 36.85°, 59.35°, 65.23°, and 77.3° are characteristic peak positions of Co_3O_4 corresponding to (220), (311), (511),

(440), and (533) planes, respectively, and thus indicates the incorporation of Co_3O_4 in the sample. The relatively reduced intensities of Co_3O_4 peak positions compared to that of pristine Co_3O_4 reported in the literature is an indicative of its phase distortion due to the presence of ZnO as its binary oxide (Xu et al. 2018). Similar behavior was noticed while reviewing the literature (El-Molla et al. 2017), which confirms the formation of highly crystalline binary oxides of Zn and Co. All diffraction peaks were found consistent with JCPDS files 65-3411 and 43-1003 for ZnO wuzrite and Co_3O_4 cubic phases, respectively. Average crystallite size of the prepared ZnO-Co_3O_4 was calculated from FWHM values using Debye Scherer`s equation is 39.09nm.

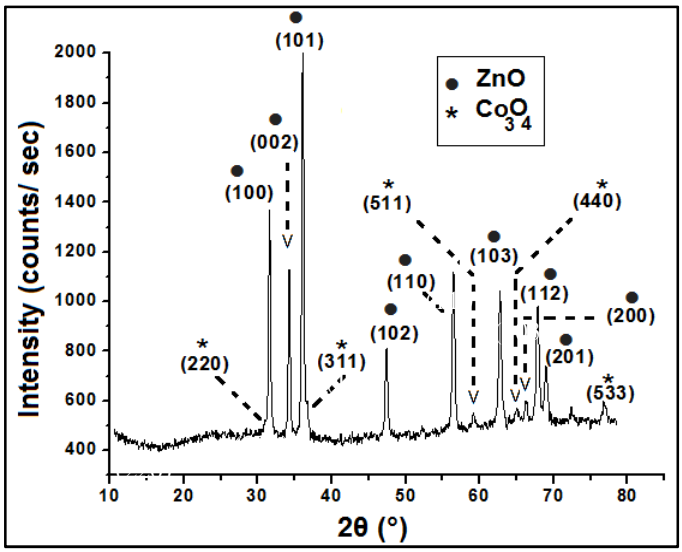

Fig. 2 X-ray diffraction (XRD) pattern of ZnO-Co_3O_4 powder

Raman analysis of ZnO-Co_3O_4 binary metal oxide

Raman spectroscopic studies were carried out to explicate the formation of ZnO-Co_3O_4 alloy so that the alloy-induced disorders can be clearly analyzed by vibrations, rotations and other low-frequency modes in a system.

Wurtzite phase of pristine ZnO is reported in the literature to occupy a distinctive region in Raman spectrum at 430 cm^{-1} corresponding to E_2(high) mode and any deviation / shift is usually associated with material impregnation (Abed et al. 2019). As shown in Fig. 3, a pronounced frequency shift of this E_2(high) peak towards 442cm^{-1} has appeared due to Co_3O_4 incorporation in the oxide structure of pure Zn (Raman shifts of 7 wt.% Co_3O_4 in ZnO optimized w.r.t. UV-Vis studies conducted for multi-layer growth optimization have been selected for discussion).

Raman shift at 330 cm^{-1} is due to multiple phonon scattering process corresponding to E_2(high)-E_2(low) mode of ZnO while the other one at 380 cm^{-1} is associated with A_1(TO) mode of ZnO. In addition, modes around 495, 530 and 630, 719 cm^{-1} are due to E_g, F_{2g}, A_{1g} phonon symmetries of Co_3O_4, in which Co^{2+} and Co^{3+}cations situated at tetrahedral and octahedral sites undergo lattice vibration in the cubic lattice, confirming the presence of spinel Co_3O_4 (Kashyap et al. 2009; Sharma et al. 2011; Stella et al. 2015).

As described in Fig. 3, Raman spectrum confirms the formation of wurtzite ZnO and cubic Co_3O_4 in the composite material, and further testifies the results of XRD patterns (Fig.2). Raman studies of ZnO-Co_3O_4 conducted by Stella et al., (2016) report almost similar modes for this binary oxide composite.

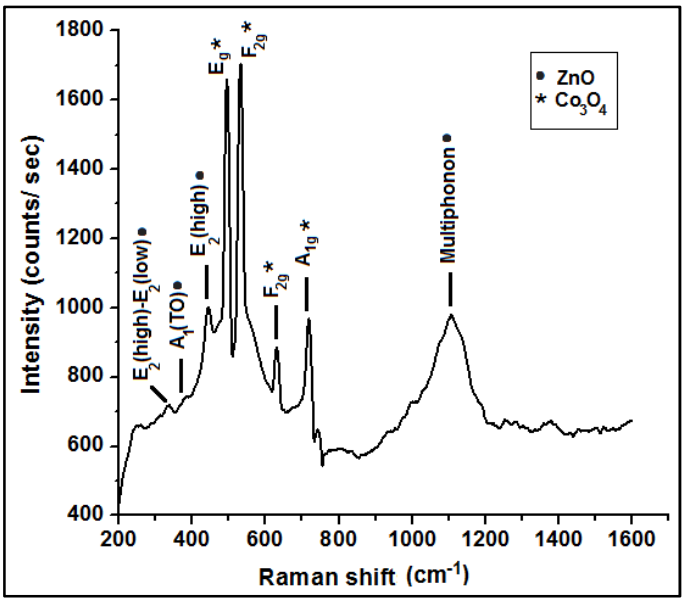

Figure 3. Raman spectorscopic shifts of ZnO-Co_3O_4 powder

Thermogravimetric analysis (TGA) of ZnO-Co_3O_4 binary metal oxide

TG analysis of the prepared ZnO-Co_3O_4 was carried out to get an insight about its thermal stability and weight change curve is presented in Fig. 4 (TGA of 7 wt.% Co_3O_4 in ZnO optimized w.r.t. UV-Vis studies conducted for layer pair growth has been selected for discussion). The curve represents high thermal stability of the prepared composite as only 5.03% of sample weight is lost in between initial decomposition temperature (181.4°C) and final decomposition temperature

(781.4°C) with a residue of 94.969% at 790.4 °C. First weight loss upto 226°C is attributed to the loss of residual water molecules, followed by second weight loss upto 406.4°C might be associated with the decomposition of residual acetate material, while slow but gradual weight loss upto 790.4°C is ascribed to combustion of residual organic material (Marin et al. 2014; Zak et al. 2011; Gill et al. 2010). Relatively similar thermogram was reported for CdO-ZnO composites by Rajaboopathi & Thambidurai (2017) thereby supporting the heat endurance capacity and high temperature resistance of the prepared ZnO-Co_3O_4 binary oxide composite.

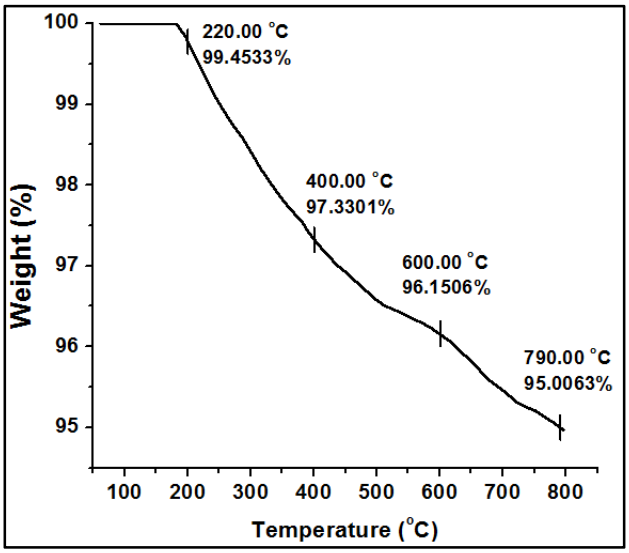

Fig. 4 TGA curve of ZnO-Co_3O_4 powder

Measuring film thickness during multilayer deposition

UV-Vis spectroscopic analysis

Multilayer buildup of PEI(PAA/ZnO-Co_3O_4)$_n$ was initiated by the deposition of a precursor cationic layer of PEI on glass substrate, followed by successive adsorption of anionic layers of PAA, and cationic layers of prepared ZnO-Co_3O_4 binary oxide composites. The thickness of bi-component thin films was measured using UV–Vis spectroscopy at wavelength (λ_{max}) 376 nm as a function of absorbance to observe the multilayer build up. Optimizations of PEI(PAA/ZnO-Co_3O_4)$_n$ film growth were made as a function of Co_3O_4 wt.% content in relation to ZnO (1-9 wt.%); ZnO-Co_3O_4 concentration in DW (1-7mg/mL); dipping time (5-50 min); followed by number of

layer pairs (n= 1-48) grown with the set of optimized parameters. The results were obtained at constant PAA concentration of 2mg/mL.

PEI/PAA complexes may have formed due to electrostatic interactions or hydrogen bonding between two polyelectrolytes (Zhang et al. 2013; Gill et al. 2010), while deposition of alternate layers of polyanion and ZnO-Co_3O_4 particles may have occurred via electrostatic interactions (Priya et al. 2009).

Fig. 5a represents the influence of varying wt. % of Co_3O_4 in ZnO (1-9wt.%) on film growth. Growth of each film was observed to follow a linear trend which indicates proper deposition of layer pairs (Ronge et al. 2015; Ismail et al. 2011). Maximum film growth as a function of absorbance was observed at 7wt.% ZnO-Co_3O_4 after which a non-linear increment followed by a sudden decline in architectural growth was observed when % weight of Co_3O_4 in ZnO was further increased to 9wt.%. This might be associated with the absence or limited availability of functional sites on polymer (PAA) surface to bound with increased Cobalt content in the binary oxide.

Fig. 5b represents the effect of ZnO-Co_3O_4 concentration (mg/mL) where the optimized architecture PEI(PAA/ZnO-Co_3O_4)$_{12}$ with 7wt.% of Co_3O_4 in ZnO was studied at varied ZnO-Co_3O_4 concentration from 1-7 mg/mL. Maximum UV-Vis absorbance was recorded at 3 mg/ml concentration. However, further increase in concentration resulted in decreased absorbance probably due to agglomeration and sedimentation of suspension particles. Another contributing factor can be electrostatic repulsion which limits further adsorption of binary oxide particles of higher concentration on the charged substrate (Vebber et al. 2019).

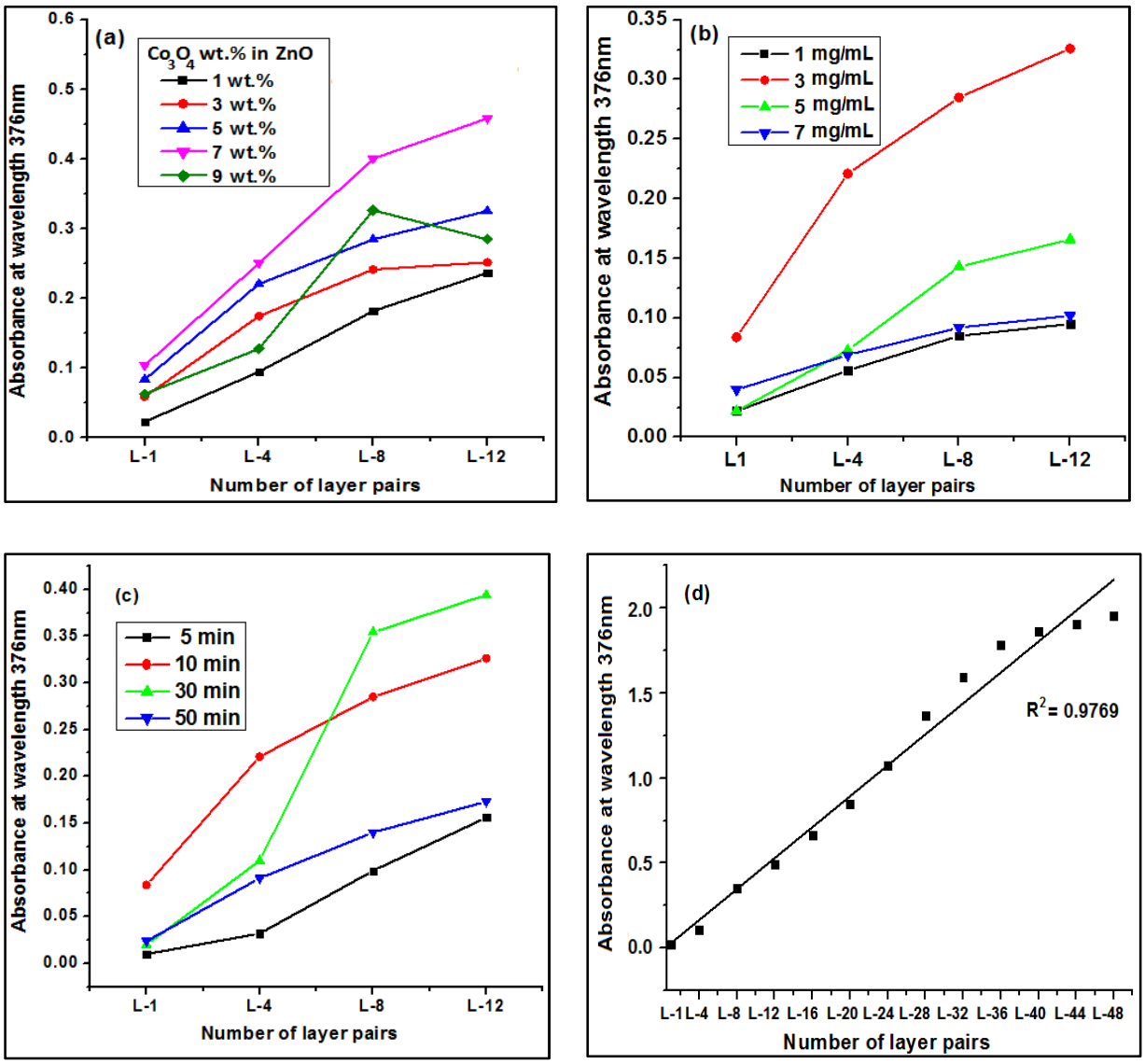

Fig. 5 UV-Vis studies for multi-layer film growth measurements by varying parameters: (a) Co_3O_4 wt.% in ZnO; (b) ZnO-Co_3O_4 concentration; (c) dipping time; (d) Number of the deposited layer pairs

Appropiate adsorption of composites and polyelectrolytes is determined by time period for which the substrates are dipped in their respective suspensions or solutions. Fig. 5c graphically represents the results obtained from studying the effect of dipping time (5-50min) on deposition of PEI $(PAA/ZnO/Co_3O_4)_{12}$ thin films. An increase in absorbance was noted as the dipping time was increased from 5-30 min, followed by decrease in absorbance for extended dipping period. This

might be attributed to the fact that reaction system attained equilibrium in 30 min which hindered further diffusion of material from solution phase towards the surface of thinfilms followed by desorption of already adsorbed particles when dipping time was further increased to 50 min.

Influence of number of deposited layer pairs on the growth of fabricated thin films is represented in Fig. 5d. Two different trends were observed for the deposited architecture: an exponential growth upto deposition of 8 layer pairs followed by stepwise linear growth upto the deposition of 8-32 layer pairs. After deposition of 36 layer pairs a plateau started to appear and film growth became relatively stable with minimal increase in absorbance from 40^{th}-48 layer pair deposition. Thus, no further deposition was carried out after 48^{th} layer pair. In multi-layer deposition reactions, linear growth pattern of deposited thin films signifies that the amount of adsorbed material is constant at consecutive cycles (as observed from 12^{th}-48^{th} layer pair deposition), while that of exponential growth shows that the amount of adsorbed material is increasing with successive cycles (as observed from 1^{st}-8^{th} layer pair deposition). Gomes et al. (2013) reported a similar trend for the deposition of bovine serum albumin (BSA)/wine LbL deposited thin films at dipping time 30 min. To give a clear insight of the mechanism involved in the optimization and buildup of current multi-layer architecture, figure 6 illustrates the schematic of multi-layer deposition of PEI(PAA/ZnO-Co_3O_4)$_n$ thinfilms.

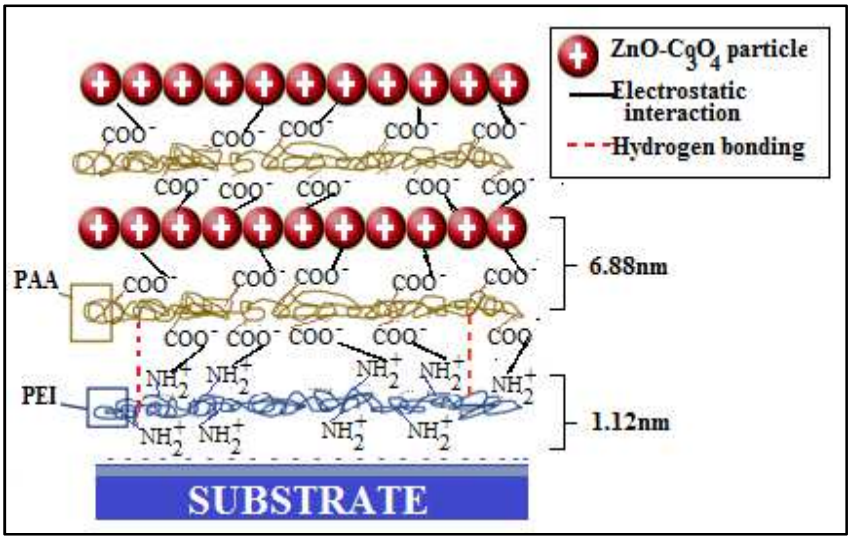

Fig. 6 Schematic representation of assembly of PEI(PAA/ZnO-Co_3O_4)$_n$ thin films

Ellipsometric Studies

Growth of thin films was also studied using Ellipsometer where increase in film growth was recorded as a function of increased film thickness (nm) using optimized architecture PEI(PAA/ZnO/Co_3O_4)$_{48}$ (7 wt.% Co_3O_4 in ZnO; ZnO-Co_3O_4 ~ 3mg/mL; dipping time ~30 min; No. of deposited layer pairs ~ 48) . As shown in Fig. 7, three different trends can be observed: an exponential increase in thickness upon deposition of first 8 layer pairs; stabilization upon deposition of 12th layer pair; and linear increase in thickness upon further deposition till 48th layer pair. This particular pattern has been reported as a feature of weak polyelectrolytes (Li et al. 2012; Gu et al. 2016). The sudden increase in film thickness upon deposition of first few layer pairs might have resulted from the diffusion of PAA into previous layer pairs (Guzmán et al. 2020). Upon deposition of specific number of layer pairs, this diffusion becomes limited as the film becomes denser, after which the linear increase in thickness was observed till 48 layer pairs with an average film thickness ~ 87 nm after which no pronounced increment was recorded. It could be anticipated that within the reaction medium, point of saturation has reached at the molecular level, as it was observed during UV-Vis studies (Gu et al. 2016). Thus, PEI(PAA/ZnO-Co_3O_4)$_{48}$ having thickness 87 nm is considered as optimized structure as given in fig. 7 where a numerical relationship between number of deposited layer pairs and increase in film thickness is presented.

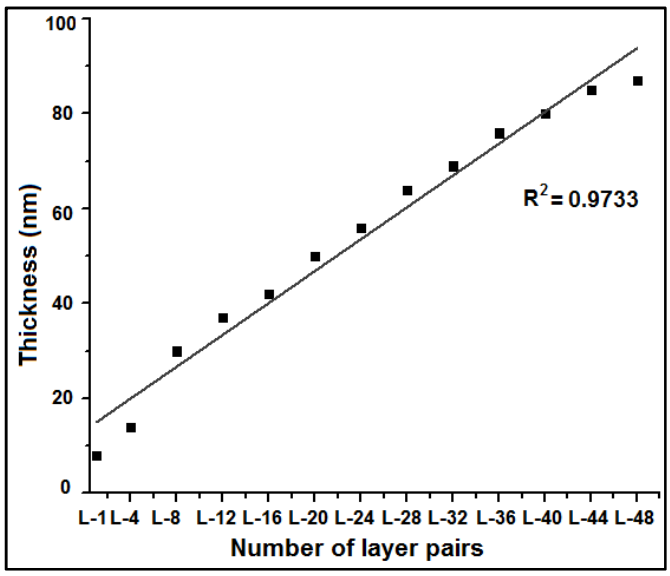

Fig. 7 Ellipsometric studies for Thickness measurements of PEI(PAA/ZnO-Co_3O_4)$_{48}$

Scanning electron Microscopy (SEM) - Energy Dispersive X-Ray (EDX) Analysis

Morphological studies were carried out to get an insight of the prepared mixed oxides of Zn and Co; their arrangement once embedded inside polymer thin films while EDX analysis was conducted to look for their elemental composition at atomic level. Fig. 8(a-e) represents the SEM micrographs and EDX based elemental compositions of particulate ZnO-Co_3O_4; PEI/(PAA/ ZnO-Co_3O_4)$_{48}$ thin films deposited on cellulose acetate filter (CAF) membranes, respectively (SEM-EDX analysis of 7 wt.% Co_3O_4 in ZnO optimized w.r.t. UV-Vis studies conducted for multi-layer pair growth has been selected for discussion).

Morphological evidences of the Co_3O_4 in its pristine existence, form tiny clusters of closely packed arrangements while that of ZnO is known to exhibit amorphous dense masses (Itteboina & Sau 2019; Panchal et al. 2019). After an insight form the literature, present research is focused to create the composite of these two oxides to identify their cumulative morphology. SEM micrographs of ZnO-Co_3O_4 (Fig. 8a, b) are clearly indicating formation of porous metal oxide particles with weak agglomerations resulting into foamy/ spongy cave like structures. This random distribution of pores is accredited to the disturbance in innate ZnO structure due to Co_3O_4 infusion at the time of their co-precipitation. This structural arrangement is in support with the literature (Sangeta et al. 2017). Morphological description of PEI/(PAA/ ZnO-Co_3O_4)$_{48}$ thinfilms @ CAF membrane is given in Fig. 8d. SEM analysis of thinfilms on porous substrate i.e. CAF is particularly selected for discussion to explain the importance the importance of selected thinfilms deposition technique i.e. “LbL deposition” due to the uniformity it provides in deposition and the tailoring properties it offers w.r.t the substrate (rough/smooth, porous/non-porous, conductive/non-conductive, etc.). As seen in Fig.8d, homogenous deposition along with fine connectivity among ZnO-Co_3O_4 particles and polymeric unit PAA covering each site of the porous filter substrate is representative of the successful deposition of multi-layered architecture PEI/(PAA/ ZnO-Co_3O_4)$_{48}$.

Furthermore, EDX analysis of the binary metal oxide and its respective thin films (Fig. 8c, e) confirm the presence of elemental C, Zn, Co and O in their respective percentages. The relatively increased percentage of C is coming from the presence of PAA polyelectrolyte as well as from the cellulosic content of the substrate. Table 2 presents the percentage weight and atomic compositions of the prepared materials.

PEI/(PAA/ ZnO-Co_3O_4)$_{48}$ on CAF membrane was tested against heavy metal adsorption of Cu (II) ions from polluted aqueous solutions, which was successfully confirmed via EDX study representing Cu peak adsorbed during the pollutant removal process as shown in Fig. 8f and Table 1. Further details of the adsorption behavior of the prepared thin films will be discussed later in the product application section (Fig. 10).

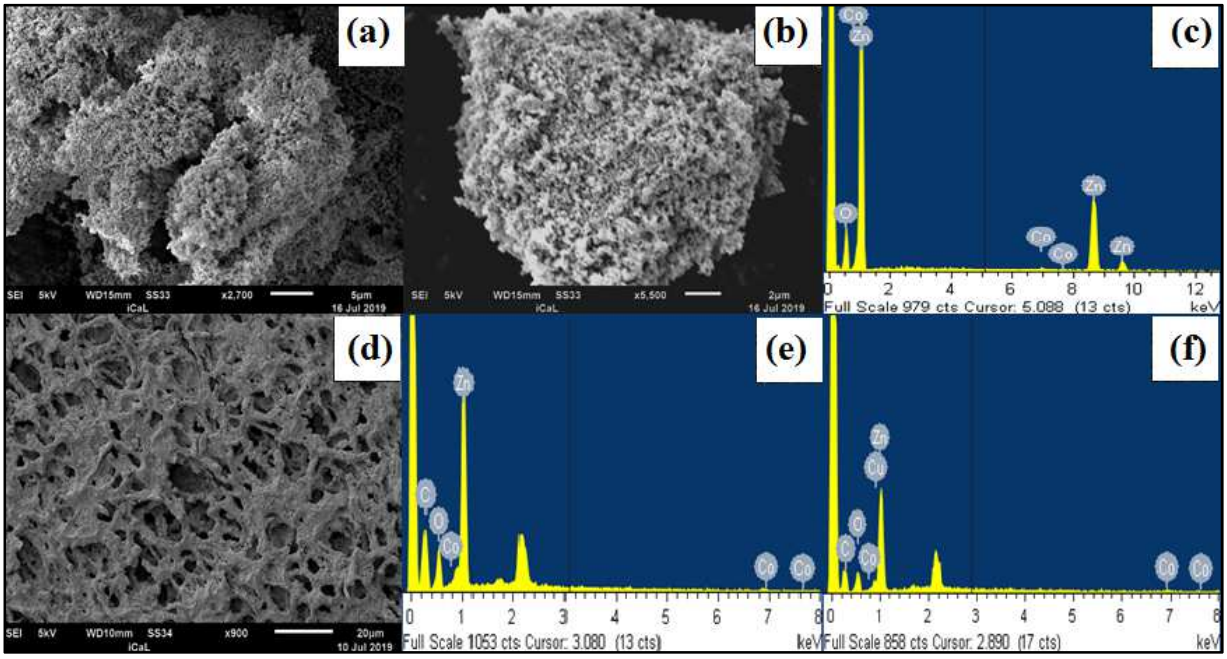

Fig. 8 SEM-EDX analyses of (a,b,c) ZnO-Co_3O_4 particles captured at 5 µm and 2 µm; (d,e) PEI(PAA/ZnO-Co_3O_4)$_{48}$ thin films multilayers deposited on CAF membrane; (f) elemental compositions recorded after Cu (II) heavy metal adsorption onto prepared thin films

Table 1 EDX analysis of ZnO-Co_3O_4 and its multi-layer thin film depositions

	ZnO-Co_3O_4 powder		**PEI(PAA/ZnO-Co_3O_4)$_{48}$**		**PEI(PAA/ZnO-Co_3O_4)$_{48}$ after Cu adsorption**	
Element	Weight%	Atomic %	Weight%	Atomic %	Weight%	Atomic %
Zn	80.53	49.61	5.74	10.39	54.06	19.36
Co	4.99	9.04	56.16	20.59	0.85	0.34
O	14.48	41.35	15.47	23.93	14.21	20.82
C	**----**	**----**	22.63	45.09	30.54	59.35
Cu	**----**	**----**	**----**	**----**	0.42	0.16
Total	100.00		100.00		100.00	

Testing the application of the designed multilayer architecture

The aim of present study was to design triple action multi-functional nanocoatings for polluted water systems which were tested for photo degradation experiments on Methylene Blue (MB) dye; batch adsorption studies of Cu (II) heavy metal ions and biocidal efficiency against *E.coli* as waterborne lethal microbe.

Photo degradation efficiency of PEI(PAA/ZnO-Co_3O_4)$_{48}$ thin films

The plot between irradiation time and percentage degradation of MB using PEI(PAA/ZnO-Co_3O_4)$_{48}$ thin films fabricated under optimal deposition conditions is represented in Figure 9a. Percentage photodegradation was calculated using UV-Vis absorbance data recorded at 665 nm. As shown in Figure 9a, % degradation was enhanced upon increase in irradiation time upto 90 minutes. No significant % degradation was recorded after this time period and thus irradiation time of 90 min was optimized to degrade MB (10ppm). Increase in degradation with increased irradiation time can be related to increase in excitation process which leads the generation of free radical oxidizers, while plateau might have resulted due to saturation of photocatalyst (Marcelino & Amorim 2019; Liu et al. 2015; Al-Shabanat & Al-Anazy 2018). The prepared architecture is found efficient to degrade 91.03% MB (10ppm) within first 90 minutes of the reaction. Present composite thin films were also studied for other MB dye concentrations (5, 10, 15, and 20 ppm)

where pronounced degradation (91.03%) with first 100 min was obtained for 10 ppm dye concentration as reported in Fig. 9a.

Reusability of a designed material significantly determines its practical application and economic viability. Therefore, in current work the methodology employed by Gokul et al. (2016), was adopted with few modifications. During each cycle fresh MB solution (10 ppm) was exposed to prepared PEI(PAA/ZnO-Co_3O_4)$_{48}$ thin films for optimized time 90 min and the procedure was repeated up to five cycles followed by analyzing aliquots *via* UV-Vis spectroscopy. As depicted in Figure 9b, the prepared architecture remained effective in degrading the highly concentrated MB dye solution with a reduction in % degradation upto 22% after five consecutive cycles of 90 min each. This might be attributed to the adsorption of degraded dye products on active sites of the prepared thin films (Saadon et al. 2016; Sapkota & Mishra 2013; Reda et al. 2017). Thus, the designed architecture can be considered as cost-effective and reusable for upto several cycles.

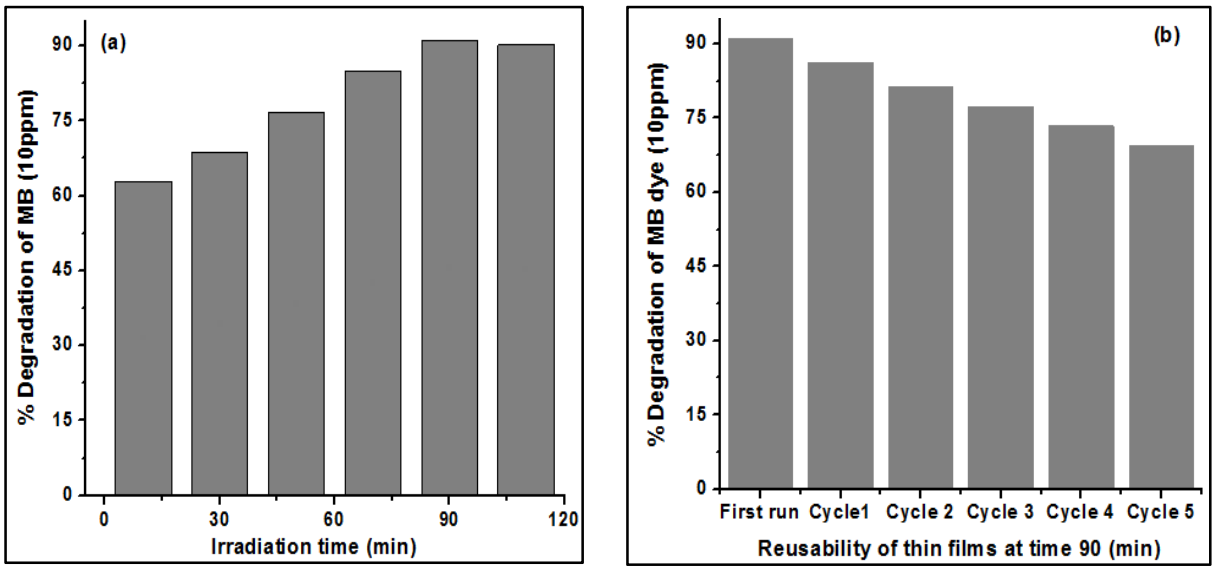

Fig. 9 Photodegradation efficiency of PEI(PAA/ZnO-Co_3O_4)$_{48}$ thin films against Methylene blue (MB) dye (10ppm) (a) At varied irradiation time; (b) Reusability of PEI(PAA/ZnO-Co_3O_4)$_{48}$ thin films at optimized time (90 min)

Heavy metal ion adsorption efficiency of PEI(PAA/ZnO-Co_3O_4)$_{48}$ thin films: porous vs non-porous substrates

Flame atomic absorption spectroscopic analysis

Adsorption potential of the multilayered PEI(PAA/ZnO-Co_3O_4)$_{48}$ thin films against heavy metal Cu (II) ions from aqueous medium was checked via FASS by depositing the optimized multilayers on flat non-porous substrate (glass) as well as on porous cellulose acetate filter (CAF) membranes. The two key parameters for batch adsorption studies are contact time between adsorbate and adsorbent and concentration of the adsorbate/pollutant. Contact time optimizations were made by varying adsorption time between 2.5-150 min (at constant initial Cu (II) concentration ~10ppm). In case of PEI(PAA/ZnO-Co_3O_4)$_{48}$ @ porous CAF membranes, maximum adsorption of 84.45% was recorded at contact time 70 min while for PEI(PAA/ZnO-Co_3O_4)$_{48}$ @ glass substrate (GS) it took 90 min to adsorb 81.27% of the similar pollutant concentration after which the system attained equilibrium for both the substrates with no profound increments in copper adsorption (Fig. 10a). Furthermore, effect of metal ion concentration was studied by varying Cu^{2+} ion concentration between 2.5-110 ppm at optimized contact times for each substrate based multilayer depositions (70 min for CAF and 90 min for GS). At 30ppm copper concentration both systems exhibited maximum adsorption potential where CAF based nanocoatings adsorb 88.93% while that of GS based nanocoatings adsorb 82.56% of the 30ppm Cu(II) from solution. Further increase in pollutant concentration did not increase % adsorption from their respective solutions as shown in Fig. 10b.

The proposed mechanism of adsorption for current research is explained as follows: Increased surface area and availability of more adsorption sites per layer pair on porous CAF substrate makes Cu (II) adsorption more effective at relatively reduced contact time compared to GS based depositions. Diffusion of metal ions from the solution phase into the initially deposited multilayers takes relatively more time in case of thin films deposited flat GS (90min) than those deposited on porous CAF (70 min). Both CAF and GS deposited thinfilms attain equilibrium after saturation of the available adsorbent's active sites after which no further movement of pollutant ion from the solution phase towards the active sites of the thinfilms was favored (Van et al. 2018).

Regeneration studies of PEI(PAA/ZnO-Co_3O_4)$_{48}$ thin films deposited on GS were conducted where Cu (II) loaded thinfilms were dipped in 0.01 M HNO_3 solution for the same time (90 min) at which

thin films exhibited maximum Cu (II) adsorption. The metal de-loading behavior of the multi layers was confirmed via FAAS and the results revealed 51.56% desorption (12.8 ppm) out of the total adsorbed metal ion content (i.e. 24.77 ppm, 82.57% of 30 ppm) (Fig. 10c). The results also reflect tunable behavior of the multi-layered thin films where pollutant loading and de-loading can significantly be done as per the choice of the operator.

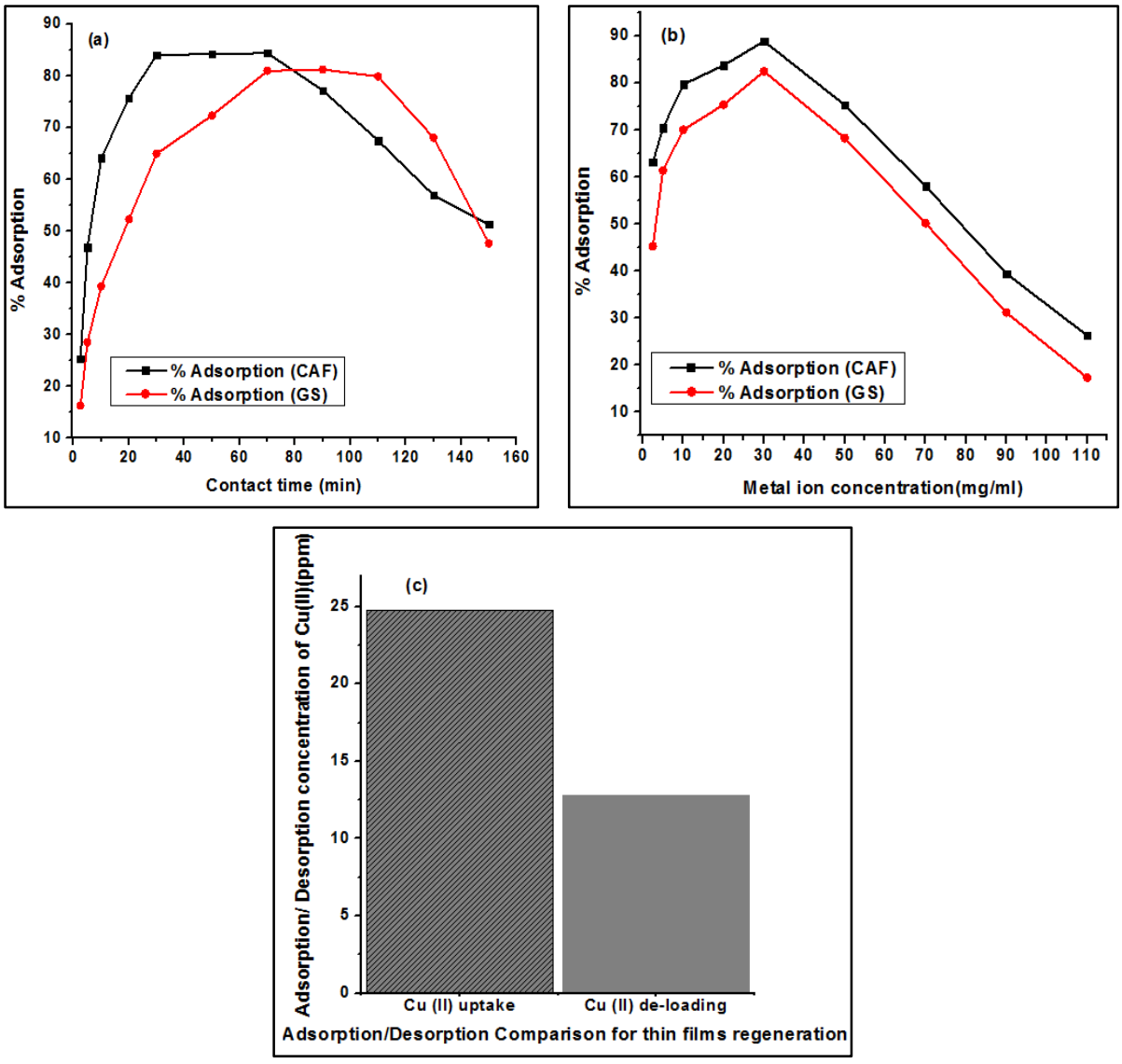

Fig. 10 Heavy metal adsorption efficiency of PEI(PAA/ZnO-Co_3O_4)$_{48}$ thin films against Cu (II) metal ions with varied (a) contact time; (b) metal ion concentrations; (c) and adsorption/ desorption comparison studies for thin films regeneration

ICP-OES studies for Cu (II) adsorption

Heavy metal adsorption potential of the PEI(PAA/ZnO-Co_3O_4)$_{48}$ deposited on CAF was also checked via ICP-OES analysis where aliquots from the Cu(II) solution with maximum adsorption capacity ~88.93 % at contact time 70 min were used for testing. The analyzed aliquots had average Cu (II) concentration of 3.87mg/l (adsorption = 87.1%) and thus confirms the uptake of 26 mg/l of Cu (II) out of the 30ppm tested solution. % adsorption results form ICP-OES studies were found close to the results obtained from FAAS studies (adsorption = 88.93%) making the presently constructed multilayers suitable for heavy metal uptake from polluted water.

To the best of our knowledge, current research and its findings are novel in demonstrating such higher concentration of heavy metal ions effectively adsorbed at relatively reduced contact time ~70min with minimum adsorbent dose ~ 30mg (3mg/ml used for 48 layer pair deposition) against Cu (II) pollutant volume ~50 ml.

Anti-microbial testing

Third appalling pollutant coming from mal-functioned drinking water facilities found lethal for human life, is water borne microbial population which is becoming resistant with each passing day (Wang et al. 2018). Considering so, antibacterial effectiveness of the designed architecture PEI(PAA/ZnO-Co_3O_4)$_{48}$ against *E. coli* was monitored at optical density OD $_{600\ nm}$ for change in absorbance with respect to time was recorded to analyze the contact kill efficiency of the prepared thinfilms. Fig. 11 is showing the kinetic growth study of *E. coli* where a persistent gradual decline with respect to time is seen from 0 to 32 hr. Per hour change in readings were recorded till first 9 hr of the contact between *E.coli* and the prepared thin films followed by an intermediate reading at 24th hr and then final reading taken at 32nd hr. Substantial effect on *E. coli* growth resistance and population decline (as function of absorbance at OD $_{600\ nm}$) was found during first 8 hr of antibacterial activity followed by prominent decline in absorbance recorded at 24th hr. It is seen that anti-microbial efficiency on *E. coli* remains almost constant from the 24th hr to the 32nd hr confirming that *E. coli* could not gain any resistance against the designed biocidal thinfilms followed by the complete expiration of the *E.coli* population. When compared with the biocidal

efficiency of other ZnO based mixed oxides reported in the literature (Kadiyala et al. 2018), currently prepared nanocoatings were found quite efficient with increased rate of biocidal efficiency at reduced time and with minimal bactericidal dose required for the successful anti-bacterial application.

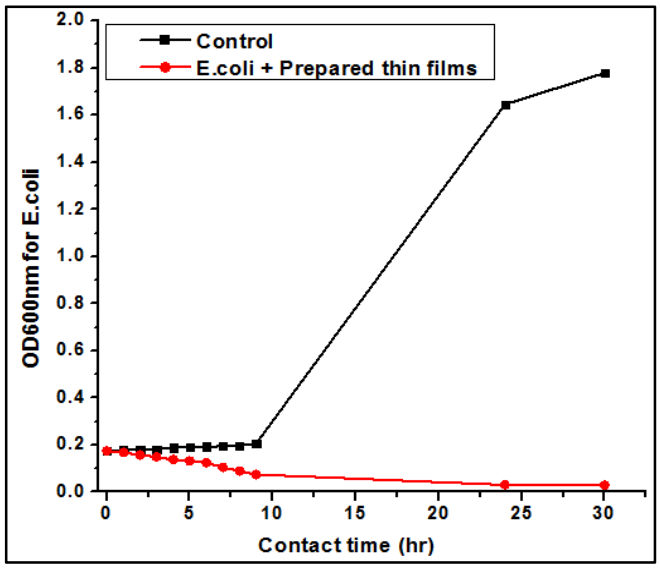

Fig. 11 Antibacterial efficiency of PEI(PAA/ZnO-Co_3O_4)$_{48}$ thin films against *E. coli*

Comparing the effect of multilayer growth on the application of the designed architecture

To materialize the efficacy of the designed architecture PEI(PAA/ZnO/Co_3O_4)$_n$, a comparison is drawn between the product application of the deposited layer pairs where n=1 and n=48 layer pairs with optimized deposition conditions were tested against selected pollutants. Significant effect of number of deposited layers on the performance of thin films is noted as tabulated in Table 2. Results highlight the importance of each deposited layer pair where the selected pollutant was allowed to infuse and pass through the multilayer architecture and it can be attributed that each successive layer pair has effectively played its role in photodegradation of dye (MB), adsorption of Cu (II) metal ion and contact killing of bacterial pathogen (*E. coli*) from the polluted water systems.

Table 2 Effect of multi-layer growth of PEI(PAA/ZnO-Co_3O_4)$_n$ on product application

Experimental Comparison	PEI(PAA/ZnO-Co_3O_4)$_{01}$	PEI(PAA/ZnO-Co_3O_4)$_{48}$
Photo degradation of MB Dye (10ppm)	18.74 %	90.22%
Heavy metal Cu (II) Adsorption (30ppm)	13.01% (CAF) 10.86% (GS)	88.93% (CAF) 82.56% (GS)
Biocidal efficiency against *E. coli* after 24hr at OD600$_{nm}$	0.167	0.029

Conclusion

Success of the present research design is evaluated through the triple action ability of PEI(PAA/ZnO-Co_3O_4)$_{48}$ hybrid nanocoatings to effectively remediate three major classes of wastewater pollutants: dyes, heavy metals and lethal bacterial colonies. Results obtained after the analytical evaluation of the designed architecture *via* XRD, Raman and FTIR spectroscopy are in line with those reported in the literature. Multilayer growth measurements *via* ellipsometer and UV-Vis depicted linear increase of film thickness. FAAS and ICP-OES results after product testing proved exceptional removal of all the tested lethal aquatic pollutants. Furthermore, recycling and regeneration capacity of the currently designed architecture makes it a favorable futuristic approach for large-scale polluted water remediation setups.

Authors' contribution: QN- Conceptualization, Experimentation, Write up, Analysis, Software and Interpretation; **ZN**- Experimentation, Write up, Interpretation; **RG-** Supervision, Conceptualization, Investigation, Reviewing and Editing; **DGS-** Investigation, Reviewing and Editing.

Availability of data and materials: All data generated or analyzed during this study are included in this article.

Declarations

Ethical approval: Not applicable

Consent for participation: Not applicable

Consent for publication: Not applicable

Competing interests: The authors declare that they have no competing interests.

References

Abbas N, Shao GN, Haider MS, Imran SM, Park SS, Kim HT (2016) Sol–gel synthesis of TiO2-Fe2O3 systems: Effects of Fe2O3 content and their photocatalytic properties J Ind Eng Chem 39: 112-120.

Abed C, Ali MB, Addad A, Elhouichet H (2019) Growth, structural and optical properties of ZnO-ZnMgO-MgO nanocomposites and their photocatalytic activity under sunlight irradiation. Mater Res Bull 110: 230-238.

Abraham N, Rufus A, Unni C, Philip D (2018) Dye sensitized solar cells using catalytically active CuO-ZnO nanocomposite synthesized by single step method. Spectrochim Acta A Mol Biomol Spectrosc 200: 116-126.

Alshabanat MN, Al-Anazy MM (2018) An experimental study of photocatalytic degradation of congo red using polymer nanocomposite films. J Chem 2018: 1-8.

Ameen S, Akhtar MS, Seo HK, Shin, HS (2014) Solution-processed CeO2/TiO2 nanocomposite as potent visible light photocatalyst for the degradation of bromophenol dye. Chem Eng J 247:193-198.

Anandan S, Sivasankar T, Lana-Villarreal T (2014) Synthesis of TiO2/WO3 nanoparticles via sonochemical approach for the photocatalytic degradation of methylene blue under visible light illumination. Ultrason Sonochem 21: 1964-1968.

Azurdia, J., Marchal, J., & Laine, R. M. (2006). Synthesis and characterization of mixed-metal oxide nanopowders along the CoO_x–Al_2O_3 tie line using liquid-feed flame spray pyrolysis. J Am Ceram Soc 89:2749-2756.

Barakat NA, Khil MS, Sheikh FA, Kim HY (2008) Synthesis and optical properties of two cobalt oxides (CoO and Co_3O_4) nanofibers produced by electrospinning process. The J Phys Chem C 112: 12225-12233.

Batool S, Gill R, Arshad M, Siddiqi H M, Qureshi SS (2018) Layer-by-layer fabrication of nacre inspired epoxy/MMT multilayered composites. J Appl Polym Sci 135: 46079.

Batool S, Gill R, Ma C, Reddy GCS, Guo W, Hu Y (2020) Epoxy-based multilayers for flame resistant flexible polyurethane foam (FPUF). J Appl Polym Sci 137: 48890.

Bodke MR, Purushotham Y, Dole BN (2018) Comparative study on zinc oxide nanocrystals synthesized by two precipitation methods. Cerâmica 64: 91-96.

Chanda A, Gupta S, Vasundhara M, Joshi SR, Mutta GR, Singh, J (2017) Study of structural, optical and magnetic properties of cobalt doped ZnO nanorods. RSC Adv 7: 50527-50536.

Decher G (1997) Fuzzy nanoassemblies: Toward layered polymeric multicomposites. Science 277: 1232-1237.

Delekar SD (2019) Sulfated TiO_2/WO_3 nanocomposite: An efficient photocatalyst for degradation of Congo red and methyl red dyes under visible light irradiation. Mater Chem Phys 225: 247-255.

El-Molla SA, Ali LI, Mahmoud HR, Ibrahim M M, Naghmash M A (2017) Effect of preparation method, loading of Co_3O_4 and calcination temperature on the physicochemical and catalytic properties of Co_3O_4/ZnO nanomaterials. Mater Chem Phys 185: 44-54.

Gill R, Batool S, Qureshi SS, Khalid R (2015) Nanofabrication of block copolymers of PDMS/polyamide having trichlorogermyl pendant using LbL technique. J Chem Soci Pak 37: 468-473.

Gill, R., Mazhar, M., Félix, O., & Decher, G. (2010). Covalent layer-by-layer assembly and solvent memory of multilayer films from homobifunctional poly (dimethylsiloxane). Angew Chem Int Ed, 49(35), 6116-6119.

Gokul, P., Vinoth, R., Neppolian, B., & Anandhakumar, S. (2017). Binary metal oxide nanoparticle incorporated composite multilayer thin films for sono-photocatalytic degradation of organic pollutants. Appl Surf Sci, 418, 119-127.

Gołąbiewska A, Kobylański M, Zaleska-Medynska A (2018) Fundamentals of metal oxide-based photocatalysis. Metal oxide based photocatalysis. Elsevier Inc Amsterdam.

Gomes MN, Brito JB, Silva JR, de Souza NC (2013) Layer-by-layer films from wine: An investigation of an exponential growth process. J Nanomater 2013: 1-7.

Gu Y, Weinheimer E K, Ji X, Wiener CG, Zacharia NS (2016) Response of swelling behavior of weak branched poly (ethylene imine)/poly (acrylic acid) polyelectrolyte multilayers to thermal treatment. Langmuir 32: 6020-6027.

Guo N, Liang Y, Lan S, et al (2014) Uniform TiO_2–SiO_2 hollow nanospheres: synthesis, characterization and enhanced adsorption–photodegradation of azo dyes and phenol. Appl Surf Sci 305: 562-574.

Guzmán E, Rubio RG, Ortega F (2020) A closer physico-chemical look to the Layer-by-Layer electrostatic self-assembly of polyelectrolyte multilayers. Adv Colloid Interface Sci 282: 102197.

Hassan HS, Elkady MF, El-Sayed EM, Hamed AM, Hussein A M, Mahmoud IM (2018) Synthesis and characterization of zinc oxide nanoparticles using green and chemical synthesis techniques for phenol decontamination. Int J Nanoelectron Mater 11: 179-194.

Hsieh CH (2007) Spherical zinc oxide nano particles from zinc acetate in the precipitation method. J Chin Chem Soci 54:31-34.

Ismail M, Bousselmi L, Zahraa O (2011) Photocatalytic behavior of WO_3-loaded TiO_2 systems in the oxidation of salicylic acid. J Photochem Photobiol A: Chem 222: 314-322.

Itteboina R, Sau TK (2019) Sol-gel synthesis and characterizations of morphology-controlled Co3O4 particles. Mater Today: Proc 9: 458-467.

Kadiyala U, Kotov, NA, VanEpps JS (2018) Antibacterial metal oxide nanoparticles: challenges in interpreting the literature. Curr Pharma Des 24: 896-903.

Kashyap SC, Bhatti KP, Chaudhary S, Pandya DK, Sharma SK (2009) Chemically Synthesized Ferromagnetic Zn1− xCoxO Nanocrystals: Raman Investigations. Synth React Inorg M 39: 216-220.

Katheresan V, Kansedo J, Lau SY (2018) Efficiency of various recent wastewater dye removal methods: a review. J Environ Chem Eng 6: 4676-4697.

Kumar SG, Rao KK (2015) Zinc oxide based photocatalysis: Tailoring surface-bulk structure and related interfacial charge carrier dynamics for better environmental applications. RSC Adv 5: 3306-3351.

Lee KM, Lai CW, Ngai KS, Juan, JC (2016) Recent developments of zinc oxide based photocatalyst in water treatment technology: A review. Water Res 88: 428-448.

Li S, Meng LM, Toprak MS, Kim D K, Muhammed M (2010) Nanocomposites of polymer and inorganic nanoparticles for optical and magnetic applications. Nano Rev 1: 5214.

Liu L, Gao ZY, Su XP, Chen X, Jiang L, Yao JM (2015) Adsorption removal of dyes from single and binary solutions using a cellulose-based bioadsorbent. ACS Sustain Chem Eng 3: 432-442.

Mahlambi MM, Ngila CJ, Mamba BB (2015) Recent developments in environmental photocatalytic degradation of organic pollutants: The case of titanium dioxide nanoparticles—A review. J Nanomater 2015: 1-29.

Marcelino RB, Amorim CC 2019 Towards visible-light photocatalysis for environmental applications: band-gap engineering versus photons absorption—a review. Environ Sci Pollut Res 26: 4155-4170.

Marin RP, Kondrat SA, Davies TE, Morgan DJ, Enache DI, Combes GB, Taylor SH, Bartley J K, Hutchings GJ (2014) Novel cobalt zinc oxide Fischer–Tropsch catalysts synthesised using supercritical anti-solvent precipitation. Catal Sci Technol 4: 1970-1978.

Panchal P, Paul DR, Sharma A, Hooda D, Yadav R, Meena P, Nehra SP (2019) Phytoextract mediated ZnO/MgO nanocomposites for photocatalytic and antibacterial activities. J Photochem Photobiol A 385: 112049.

Patil SM, Deshmukh SP, More KV, Shevale V B, Mullani SB, Dhodamani AG, Deleka SD (2019) Sulfated TiO_2/WO_3 nanocomposite: An efficient photocatalyst for degradation of Congo red and methyl red dyes under visible light irradiation. Mater Chem Phys 225: 247-255.

Pedanekar RS, Shaikh SK, Rajpure KY (2020) Thin film photocatalysis for environmental remediation: A status review. Curr Appl Phys 20: 931-952.

Priya DN, Modak JM, Raichur AM (2009) LbL fabricated poly (styrene sulfonate)/TiO_2 multilayer thin films for environmental applications. ACS Appl Mater Interface 1: 2684-2693.

Rajaboopathi S, Thambidurai S (2017) Green synthesis of seaweed surfactant based CdO-ZnO nanoparticles for better thermal and photocatalytic activity. Curr Appl Phys 17: 1622-1638.

Reda GM, Fan H, Tian H (2017) Room-temperature solid state synthesis of Co_3O_4/ZnO p–n heterostructure and its photocatalytic activity. Adv Powder Technol 28: 953-963.

Rongé J, Bets J, Pattanaik S, Bosserez T, Borellini S, Sree SP, Decher G, Martens J (2015) Tailoring preparation, structure and photocatalytic activity of layer-by-layer films for degradation of different target molecules. Catal Today 246: 28-34.

Saadon S, Sathishkumar P, Yusoff AR, Wirzal MD, Rahmalan MT, Nur H (2016) Photocatalytic activity and reusability of ZnO layer synthesised by electrolysis, hydrogen peroxide and heat treatment. Environ Technol 37: 1875-1882.

Sangeeta M, Karthik KV, Ravishankar R, Anantharaju KS, Nagabhushana H, Jeetendra K, Vidya YS, Renuka L (2017) Synthesis of ZnO, MgO and ZnO/MgO by solution combustion method: characterization and photocatalytic studies. MaterToday 4: 11791-11798.

Sapkota BB, Mishra, SR (2013) A simple ball milling method for the preparation of p-CuO/n-ZnO nanocomposite photocatalysts with high photocatalytic activity. J Nanosci Nanotechnol 13: 6588-6596.

Sharma PK, Kumar M, Pandey AC (2011) Green luminescent ZnO: Cu 2+ nanoparticles for their applications in white-light generation from UV LEDs. J Nanopart Res 13: 1629-1637.

Stella C, Soundararajan N, Ramachandran K (2015) Structural, optical, and magnetic properties of Mn and Fe-doped Co_3O_4 nanoparticles. AIP Adv 5: 087104.

Stella C, Soundararajan N, Ramachandran K (2016) Chunk shaped ZnO/ Co_3O_4 nanocomposites for ethanol sensor. Adv Mater Lett 7: 652-658.

Tang CW, Wang CB, Chien SH (2008) Characterization of cobalt oxides studied by FT-IR, Raman, TPR and TG-MS. Thermochim Acta 473: 68-73.

Van TV, Park D, Lee YC 2018 Hydrogel applications for adsorption of contaminants in water and wastewater treatment. Environ Sci Pollut Res 25: 24569-24599.

Vebber MC, da Silva Crespo J, Giovanela M (2019) Self-assembled thin films of PAA/PAH/TiO_2 for the photooxidation of ibuprofen. Part I: Optimization of photoactivity using design of experiments and surface response methodology. Chem Eng J 360: 1447-1458.

Wang SY, Han DC, Song C, Li MN, Afzal MZ, Wang SG, Sun XF 2019 Membrane biofouling retardation by zwitterionic peptide and its impact on the bacterial adhesion. Environ Sci Pollut Res 26: 16674-16681.

Xiao S, Zhao L, Leng X, Lang X, Lian J (2014) Synthesis of amorphous TiO_2 modified ZnO nanorod film with enhanced photocatalytic properties. Appl Surf Sci 299: 97-104.

Xu H, Shi M, Liang C, Wang S, Xia C, Xue C, Hai Z, Zhuiykov S (2018) Effect of zinc acetate concentration on optimization of photocatalytic activity of p-Co_3O_4/n-ZnO heterostructures. Nanoscale Res Lett 13: 1-16.

Yusan S, Bampaiti A, Aytas S, Erenturk S, Aslani MA (2016) Synthesis and structural properties of ZnO and diatomite-supported ZnO nanostructures. Ceram Int 42: 2158-2163.

Zak AK, Abrishami ME, Majid WA, Yousefi R, Hosseini SM (2011) Effects of annealing temperature on some structural and optical properties of ZnO nanoparticles prepared by a modified sol–gel combustion method. Ceram Int 37: 393-398.

Zhang Y, Rhim JW, Feng, X (2013) Improving the stability of layer-by-layer self-assembled membranes for dehydration of alcohol and diol. J Membr Sci 444: 22-31.